Science
AAAS

Supplementary Materials for

Isotopic evidence of long-lived volcanism on Io

Katherine de Kleer *et al.*

Corresponding author: Katherine de Kleer, dekleer@caltech.edu

DOI: 10.1126/science.adj0625

This PDF file includes:

Materials and Methods
Supplementary Text
Figs. S1 to S6
Tables S1 to S5
References

Materials and Methods

Observations

Observations were made with ALMA of Io's leading and trailing hemispheres on UT 2022 May 24 and 2022 May 18 (respectively) through program 2021.1.00849.S. QSO B0420-0127 and QSO B2251+155 were observed for flux and bandpass calibration. The time on source was 1h40m for the leading hemisphere observation, and 50 minutes for the trailing hemisphere observation, because better weather conditions allowed the desired SNR to be obtained in a shorter time. Parameters of the observations and Io's geometry at the time are given in Table S1. For the leading hemisphere observation, Io rotated 28 degrees during the observation, which smears the data by 0″.23 in the rotation direction; this is more than half the spatial resolution, but does not affect our interpretation because all presented spectra are averaged over regions larger than the spatial resolution.

The observations were conducted while ALMA was in its C-4 antenna configuration, which provides a spatial resolution of about a quarter to a third of Io's diameter (~1000 km) at the frequencies of observation. The maximum baselines were 780 and 740 m for the leading and trailing hemisphere observations respectively.

The observations used ALMA's Band 8 receivers, operating between 416 and 432 GHz. Within this frequency coverage we selected 13 spectral windows, each with a frequency resolution of 244 kHz (corresponding to a velocity resolution of 170 m s^{-1}) and a bandwidth of either 235 or 118 MHz, for a total recorded bandwidth of 1.5 GHz. Band 8 covers rotational lines of all 4 targeted species (SO_2, SO, NaCl, KCl) and their isotopologues in a single spectral set-up (Table S2). ALMA's frequency tunings were set to track the changing line-of-sight velocity of Io during the observations, so there is no spectral smearing provided the tracking uses an ephemeris sampled at sufficient precision. For these observations the ephemeris (*35*) was sampled at 10 minute intervals; the resulting spectral smearing is < 2 kHz, which is a small fraction of the spectral resolution. The full width at half maxima for the observed lines are in the range of 0.6 to 1.0 MHz for the sulfur-bearing species and 0.95-1.15 MHz for the chlorine-bearing species. A tuning error resulted in some of the spectral windows being tuned incorrectly for the leading hemisphere observation such that two SO_2 lines (430.229 and 430.232 GHz) were not covered by that observation. These lines are not used in our analysis.

Data reduction

The data were processed through the standard ALMA pipeline (*36*) to produce a calibrated measurement set (MS) containing the interferometric visibilities, which are the amplitude and phase of the cross-correlated signal between each pair of antennas. The line-free spectral channels across all spectral windows were split out to produce a continuum MS. This continuum MS was self-calibrated (*37*) and imaged with the CASA software (*38, 39*) using an iterative procedure. First, a continuum limb-darkened disk the size of Io at the time of observation was produced and converted to visibilities; a limb darkening parameter of 0.2 was used, but the final image is only weakly sensitive to the choice of limb darkening parameter. The data were then phase calibrated using the limb-darkened disk model visibilities, and imaged using the same

model as a starting point for the CLEAN deconvolution algorithm (*40*). The self-calibration and CLEAN deconvolution process was then repeated, using the output of the previous self-calibration and imaging round as the starting point for the subsequent iteration. In each round, the self-calibration was performed using an increasingly shorter solution interval, and the CLEAN algorithm was employed using an increasingly deep threshold. We used three iterations of self-calibration and deconvolution; further iterations did not improve the SNR of our images.

We applied the phase calibration derived from the continuum data (described above) to the continuum-subtracted spectral line data, then imaged each channel in the spectral line data channel separately. This produced a spectral data cube for each spectral window with ~0″.28 resolution and a spectral sampling of 244 kHz, and a frequency-averaged continuum image at ~0″.28 resolution. Figures S1 and S2 show the continuum-subtracted image integrated over each spectral line listed in Table S2. We find that each spectral line from a single species, including both isotopologues, has the same spatial distribution, which indicates that the measured spatial distributions of the species are not biased by artifacts.

The 1D spectrum in each spectral window was extracted using an aperture that includes all pixels that are 5% of the peak continuum level or higher in the continuum image. This produces an aperture whose diameter is 1.3× the diameter of Io, i.e., extending one resolution element beyond the edge of Io.

The flux density uncertainties were estimated in two ways. First, a 1D spectrum was extracted in a region absent of sources, in exactly the same way as for the source and using the same aperture size; the standard deviation of the spectrum across each spectral window was used as an estimate of the noise in that spectral window. Second, the standard deviation of the spectrum of Io in spectral regions without apparent spectral lines was calculated, again providing a noise estimate per spectral window. We adopt the more conservative uncertainties derived from the latter method, because it incorporates the thermal noise from Io's continuum. The first method gave uncertainties that were a factor of 1 to 3 lower, which we regard as under-estimates. The degree of bandpass calibration noise varies between spectral windows, and is non-negligible in some windows. The bandpass calibrator spectrum was smoothed using a frequency width of 7.8 MHz. This smoothing reduces the noise introduced by the bandpass calibrator, and although it can introduce spectral artifacts, such artifacts would be similar in width to the smoothing window and hence much broader than Io's emission lines. The uncertainties on the datapoints incorporate this noise, which is particularly high in the spectral windows containing the lines at 419.640, 428.298, 429.863, 429.952, and 420.887 GHz. The 1σ noise is shown in Figures 2 and 3 and incorporated into the maximum-likelihood calculations (see below).

Overview of modeling and retrievals

To determine the isotope ratios for sulfur and chlorine, we found best-fitting model parameters by fitting a forward model to the observations as follows. Model spectra were generated using a radiative-transfer model for the atmosphere of Io (*8, 9*), which we updated to add additional species. Our model includes opacity from SO_2, SO, NaCl, and KCl, including the ^{32}S and ^{34}S isotopes of sulfur and the ^{35}Cl and ^{37}Cl isotopes of chlorine. Models were fitted to the data using a Nelder-Mead minimization algorithm as implemented in the `optimize` package in the SCIPY software (*41*). Once the best-fitting solution was determined, we used the EMCEE Markov chain

Monte Carlo (MCMC) Ensemble sampler (*42*) to explore the model parameter space and determine the uncertainties on the best-fit parameters. Additional details on each of these steps are given below.

The parameter values that correspond to the maximum likelihood values output by the MCMC simulations match the best-fitting values found by the minimization, with differences well below 1σ. We report the resulting parameter uncertainties as the 1σ range measured from the posterior probability distributions output by the MCMC simulations. Table 1 reports the best-fitting parameters and MCMC-derived uncertainties for all free parameters in the models.

Emission line selection and treatment

For the radiative-transfer modeling, the line frequencies and strengths were adopted from the Cologne Database for Molecular Spectroscopy [CDMS (*43, 44*)]. We also tested line lists from the JPL Molecular Spectroscopy repository (*45*), but found they did not match the observed line positions in our datasets for any species except $^{32}SO_2$ and $^{34}SO_2$. The CDMS frequencies for the lines of the sulfur-bearing molecules agree with our observations after accounting for the line-of-sight velocity of Io. For NaCl, KCl, and their isotopologues, we observed an additional velocity shift that we ascribe to bulk motion of the gas and included as a free parameter in our model fitting. The observed ~100 m s^{-1} velocity shift is the same across all chlorine-bearing species within each dataset; it is smaller than the velocities of Io's largest class of plumes [500-1000 m s^{-1} (*46*)]. A velocity shift parameter is not included in the SO_2 model because the line positions match the expected frequencies from CDMS. The velocity difference between the chlorine- and sulfur-bearing species could arise because SO_2 and SO are more uniformly distributed, such that gas velocity components produce line broadening rather than a frequency shift. The broadening of the SO_2 and SO lines due to Io's rotational motion is included in the model (see below). The velocity shifts for the chlorine-bearing gasses are unlikely to be due to line list errors, because the shift is the same across NaCl and KCl lines (per dataset), whereas line list errors introduce offsets that differ between lines but are the same between datasets (per line). The frequency errors that would be introduced by using the JPL line lists are much larger than the observed frequency shifts due to gas velocity.

The strengths of the emission lines are sensitive to temperature, and the temperature profile in Io's atmosphere is poorly known. The isotope ratio also varies with altitude due to gravitational stratification. To determine the isotope ratio, we therefore used only the two lines of $^{32}SO_2$ (418.815 and 429.863 GHz) that are sensitive to the same low atmospheric altitudes as the $^{34}SO_2$ lines. The other $^{32}SO_2$ lines covered by our data, as well as those used for the previous isotope ratio measurement (*15*), have higher line opacities such that emission arises predominantly from higher altitudes than the $^{34}SO_2$ lines are primarily sensitive to. This is particularly true near the limb where the path length through the atmosphere is longest. This is illustrated in Figure S3, which shows the contribution functions calculated from the model opacities at line center for the $^{32}SO_2$ and $^{34}SO_2$ lines targeted in our observations, compared to those used for the previous isotope ratio measurement. Particularly near the limb, all the $^{32}SO_2$ lines used in the past work, and most of the $^{32}SO_2$ lines covered by our data, are sensitive to different altitudes than the $^{34}SO_2$ lines.

The SO_2 gas temperature is tightly constrained by our observations because the SO_2 model fitting includes six emission lines from high to low excitation (Table S2). Temperature affects both the line widths and the relative strengths of the lines. If each line were fitted independently, the temperature would be degenerate with column density and with the velocity distribution of the gas, leading to much larger uncertainties. However, because we fit multiple lines simultaneously, the best-fitting temperature is constrained by the relative line strengths. The resulting best-fitting temperature, in combination with Io's rotation, then determines the model line widths. The imperfect match between the model line widths and some of the observed spectra (Fig. 2) could arise from velocity components (e.g. from winds or plumes) that are not included in our model.

Model atmosphere geometry and line opacity

To determine a disk-integrated model spectrum for comparison with the data, we modeled the emission from Io's atmosphere as a function of latitude and longitude, accounting for the dependence of atmospheric path length on emission angle and the Doppler shift corresponding to Io's solid-body rotation at each latitude and longitude. The model was output with a range of spatial resolutions, from which we selected the coarsest model resolution that did not result in a disk-integrated spectrum that differed substantially from that produced by higher resolution models. Based on this criterion, we selected models generated with a spatial resolution of 0″.06 (about 6% of Io's diameter), which were then spatially integrated to produce a disk-integrated model spectrum. Changing the spatial resolution of the model causes minor changes in the derived column densities, but does not affect the derived isotope ratios.

For the $^{34}S/^{32}S$ model fitting, we assumed that Io's atmosphere is homogeneous in latitude and longitude. Figure 1 indicates that the observed fractional coverage (fraction of the surface area of Io above which there is SO_2 gas) is closer to ~50%. If the lines are optically thin, there is a linear trade-off between column density and fractional coverage: if column density is increased and fractional coverage decreased proportionally, the model line strength remains the same. This is the case provided the fractional coverage is above ~15%. Our assumption of uniform coverage therefore does not impact the derived isotope ratio, but it does affect the derived column densities.

For NaCl and KCl, the fractional coverage is unclear from the images. Figure S3 shows contribution functions that have the same disk-integrated column for the cases of 20% and 5% fractional coverage, demonstrating that if these species exhibit a lower fractional coverage and higher column density, the observed emission is coming from higher altitudes than if the species are more uniformly distributed across Io. If the fractional coverage is below ~10% there is enough opacity in the $Na^{35}Cl$ line that it no longer traces emission from the same altitudes as the $Na^{37}Cl$ line. This necessitates our inclusion of fractional coverage as a free parameter in the chlorine model fitting; if a broad range of fractional coverages is allowed by the data, the effect is to increase the derived uncertainties on all parameters that are correlated with fractional coverage. In our analysis, including this free parameter primarily increases the uncertainties on the gas column densities, because the best-fitting models are in a region of the parameter space where opacity is low and the derived isotope ratio is not strongly impacted.

As an additional check of whether opacity effects may bias the derived isotope ratios, we extracted spectra from localized regions on Io's disk with both low and high path lengths (disk center and low-latitude limbs, respectively) then applied the sulfur model fitting. For the chlorine model fitting, we performed the same check using spectra from both fainter and brighter emission regions. These tests used circular apertures with 0″.3 diameters, shown in Fig. S4, to extract the spectra. The best-fitting parameters for each region are given in Table S3. This test assumes a coverage fraction of 1.0 within the 0″.3 aperture. Some of the NaCl and KCl emission occurs very close to the limb. We find that the derived column densities are sensitive to the exact emission angle used in the models, so should be interpreted with caution, but the derived isotope ratios are not sensitive to this parameter. The results of this test show that the $^{34}S/^{32}S$ and $^{37}Cl/^{35}Cl$ ratios derived from all spectra extracted within a given hemisphere differ by $<1.5\sigma$ from the values derived from the disk-integrated spectra. The lack of systematic differences in the isotope ratios derived for low and high emission regions indicates that local opacities do not bias our derived isotope ratios. For the best-fitting atmospheric parameters and model resolution adopted above, the optical depths of all lines are <0.1 over most of the surface, and always <0.5 for the sulfur-bearing species and <0.7 for the chlorine-bearing species (with the highest values being for the strongest lines at the limbs).

The lines of $Na^{35}Cl$ and $Na^{37}Cl$ are detected at a much higher SNR than $K^{35}Cl$ and $K^{37}Cl$, due to the higher abundance of NaCl relative to KCl. Therefore the chlorine model fitting is dominated by NaCl; using the $Na^{35}Cl$ and $Na^{37}Cl$ lines alone gives the same $^{37}Cl/^{35}Cl$ ratio, within the 1σ uncertainties, as using both NaCl and KCl. The Na/K ratios for both hemispheres, including the disk-integrated and local analyses, are all in the range 3 to 10, consistent with previous studies (*14*).

Examples of derived uncertainties

Figure S5 shows a random selection of model spectra drawn from the posterior probability distribution, compared to the observed sulfur data for the trailing hemisphere, to illustrate the variations in the spectra produced by varying the parameters within their uncertainties. Figure S6 shows models in which the SO_2 column density is fixed at its best-fitting value but the $^{34}S/^{32}S$ ratio is varied from 0.040 (below the Solar System average) to 0.080 (above our best-fitting value).

Supplementary Text

Patera co-located with chlorine-bearing gasses

Our models indicate that NaCl and KCl have high gas temperatures, and Fig. 1 shows they are localized to discrete locations. As discussed in the main text, we interpret them as only present in volcanic plumes. For each of the two dates of observation, we determined the position of each source in the NaCl images and converted it to a latitude and longitude on Io using the geometry at the time of observation (Table S1). The latitudes and longitudes of the sources marked in Fig. 1 are given in Table S4. The uncertainties on the latitudes and longitudes were determined by

calculating the latitude and longitude of every pixel within a 10×10 pixel box (roughly one resolution element on each side) surrounding the determined source center, then taking the standard deviation within the box. We investigated whether these correspond to known surface features (*47*). Table S4 lists the most likely patera as well as all paterae that fall within the 1σ uncertainties.

Volcanic activity at Kurdalagon Patera (consistent with location 1 in Figure 1), is thought to have been at least partially responsible for the massive brightening of Jupiter's sodium nebula in early 2015 (*48*); our identification of NaCl gas at the location of the patera is consistent with this connection because it suggests that the style of volcanism taking place at Kurdalagon Patera produces Na-bearing gas. However, infrared images taken simultaneously with our ALMA observations on 2022 May 24 (*49*) do not show thermal emission at the latitudes and longitudes where we observe NaCl and KCl gasses. If the regions of high NaCl and KCl gas density are indeed volcanic plumes, they originate from volcanic centers that are not actively extruding large volumes of lava.

Rayleigh distillation model

We use a Rayleigh distillation model to relate the present-day ratio of two isotopes to the fraction of material that has been lost from the system over time. This relationship is quantified through the Rayleigh equation, which is $^{34}R = {}^{34}R_0 f^{{}^{34}\alpha_{\mathrm{loss}}-1}$ for the ^{34}S and ^{32}S sulfur isotopes. We use this to determine the value of f, the fraction of Io's original sulfur inventory remaining at present day, based on our measured ^{34}R.

Rayleigh fractionation entails the progressive and irreversible removal of material from a system (referred to as a reservoir). We assume an initial ^{34}S/^{32}S ($^{34}R_0$) for our system and a value for the fractionation factor ($^{34}\alpha_{\mathrm{loss}}$), which describes the instantaneous isotopic partitioning between the modelled system and each packet of material removed at each time step. The Rayleigh distillation framework assumes that i) the material is being removed continuously, and ii) the residue is well mixed.

For the case of sulfur on Io, we propose that the well-mixed system consists of all of Io's sulfur that is not in the moon's core. It is also possible that a smaller shallow system, consisting just of Io's atmosphere and crust (and perhaps some portion of the upper mantle), is mixed more rapidly, due to shallow re-melting of surface frosts recycled into the crust. In such a scenario, this smaller well-mixed sulfur reservoir would become isotopically fractionated more rapidly than the full mantle plus crust system. However, to maintain the crust-atmosphere reservoir, mantle material would need to be continuously injected to balance Io's mass loss rate of 1000 to 3000 kg s^{-1}. This injection of essentially unfractionated mantle material would buffer the near-surface system such that the atmospheric ^{34}S/^{32}S could not become highly fractionated: the atmospheric ^{34}S/^{32}S would take values between those of steady-state and Rayleigh fractionation scenarios (*20*). Fractionation in the shallower, smaller system could only produce a highly fractionated atmospheric ^{34}S/^{32}S if there is no addition of unfractionated mantle. We consider that scenario highly unlikely, given the observed mantle-derived volcanism and the amount of sulfur input into the crust that is required to balance Io's mass loss.

By assuming the well-mixed reservoir consists of all Io's sulfur that is not in the core, our model calculation also requires that there is no sulfur exchange between the core and mantle. The sulfur isotopic fractionation factor between metal and silicates is close to 1 (*50*), so we expect that the formation of Io's core left it with the moon's initial sulfur isotope composition. If Io's core supplies sulfur to the mantle, this provides a source at Io's initial $^{34}S/^{32}S$ ratio and therefore lowers the average $^{34}S/^{32}S$ ratio of the sulfur that is available for loss. This would therefore require even greater sulfur loss to explain our measurement.

The derived fraction of sulfur lost from Io depends on our adopted initial isotope ratio $^{34}R_0$ and $^{34}\alpha_{loss}$. As discussed in the main text, potential deviations in the $^{34}S/^{32}S$ ratio of Io-forming material from the Solar System average are expected to be four orders of magnitude smaller (in $\delta^{34}S_{VCDT}$) than our observed fractionation. Adopting the Solar System average for $^{34}R_0$ is therefore not a large source of uncertainty. The value we adopt for $^{34}\alpha_{loss}$ assumes that all loss takes place at or above an exobase located at 600 km altitude. The altitude of the exobase is uncertain and could be as low as 100 to 200 km (*51, 52*). During Io's night time, the exobase might be at the surface itself. If we adopted an exobase at a lower altitude than 600 km, it would result in an $^{34}\alpha_{loss}$ value closer to 1. This would put our loss fraction derived from the Rayleigh equation at the upper end of our reported range but does not qualitatively change our conclusions.

In our implementation of the Rayleigh model, we assume a constant fractionation factor, $^{34}\alpha_{loss}$. On Io, however, $^{34}\alpha_{loss}$ probably changes on diurnal, seasonal, and stochastic timescales, as Io's exobase altitude changes in response to changing atmospheric densities. We made the simplifying assumption of a fixed altitude because we expect the exobase is typically at or below our adopted value, such that any deviation from our assumption would result in the same conclusion, or even greater sulfur loss.

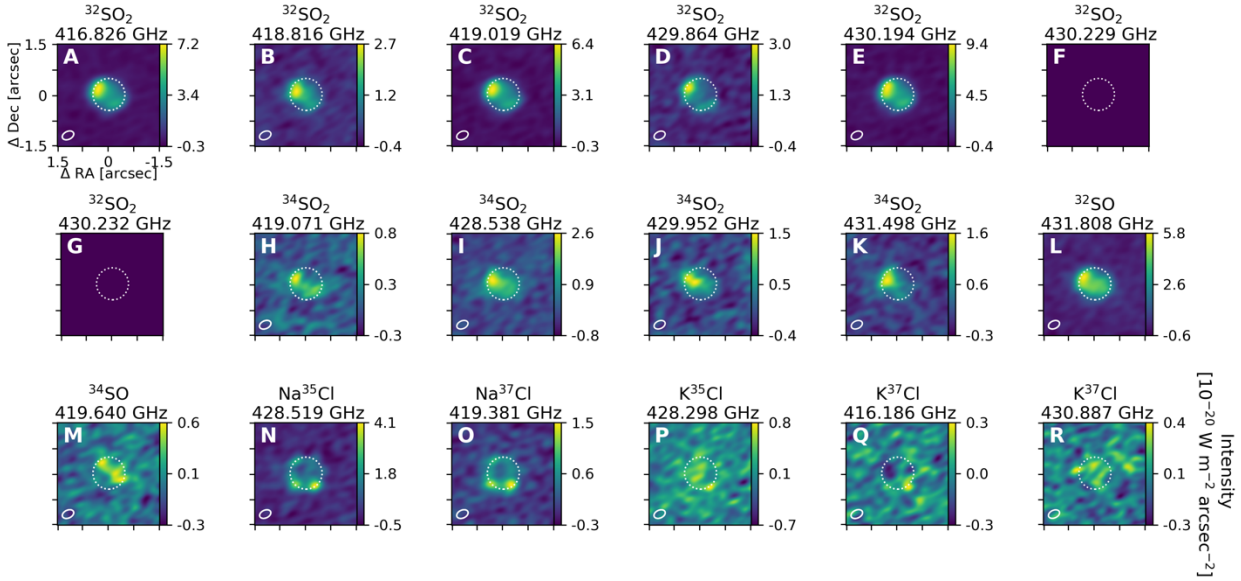

Fig. S1. **Distributions of all observed molecular emissions from Io's leading hemisphere.** Same as Figure 1, but for all the lines we observed (listed in Table S2) on the leading hemisphere for (**A-G**) $^{32}SO_2$, (**H-K**) $^{34}SO_2$, (**L**) ^{32}SO, (**M**) ^{34}SO, (**N**) $Na^{35}Cl$, (**O**) $Na^{37}Cl$, (**P**) $K^{35}Cl$, and (**Q-R**) $K^{37}Cl$. A tuning error led to no recorded data for the SO_2 lines at (**F**) 430.229 and (**G**) 430.232 GHz. Colorbars are in the intensity units given in Panel R.

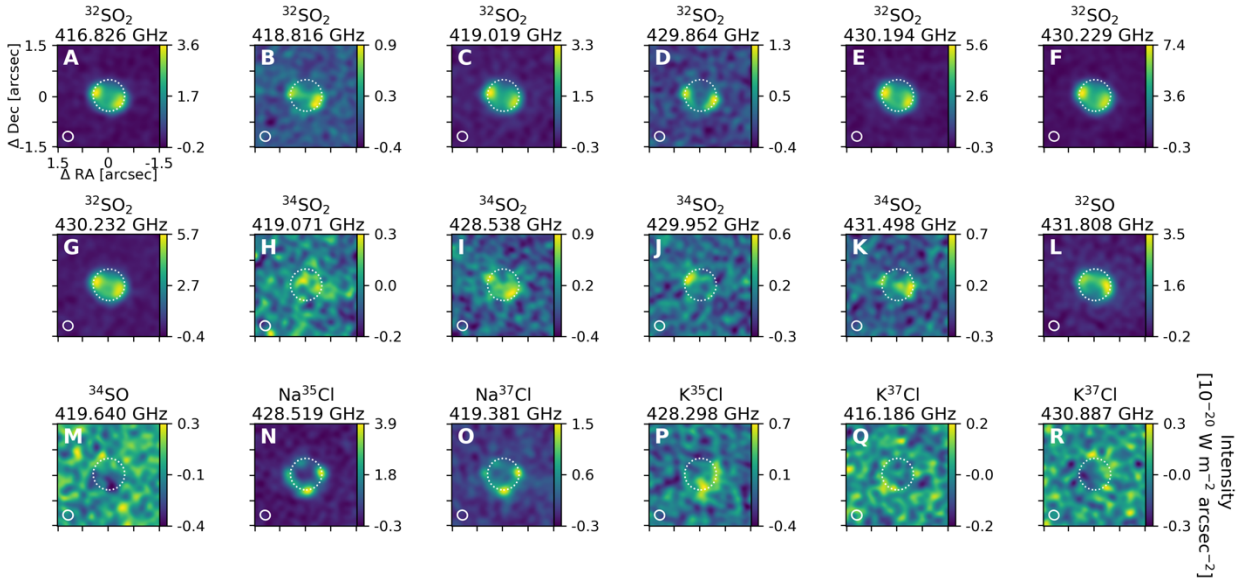

Fig. S2. **Distributions of all observed molecular emissions from Io's trailing hemisphere.** Same as Fig. S1, but for the trailing hemisphere.

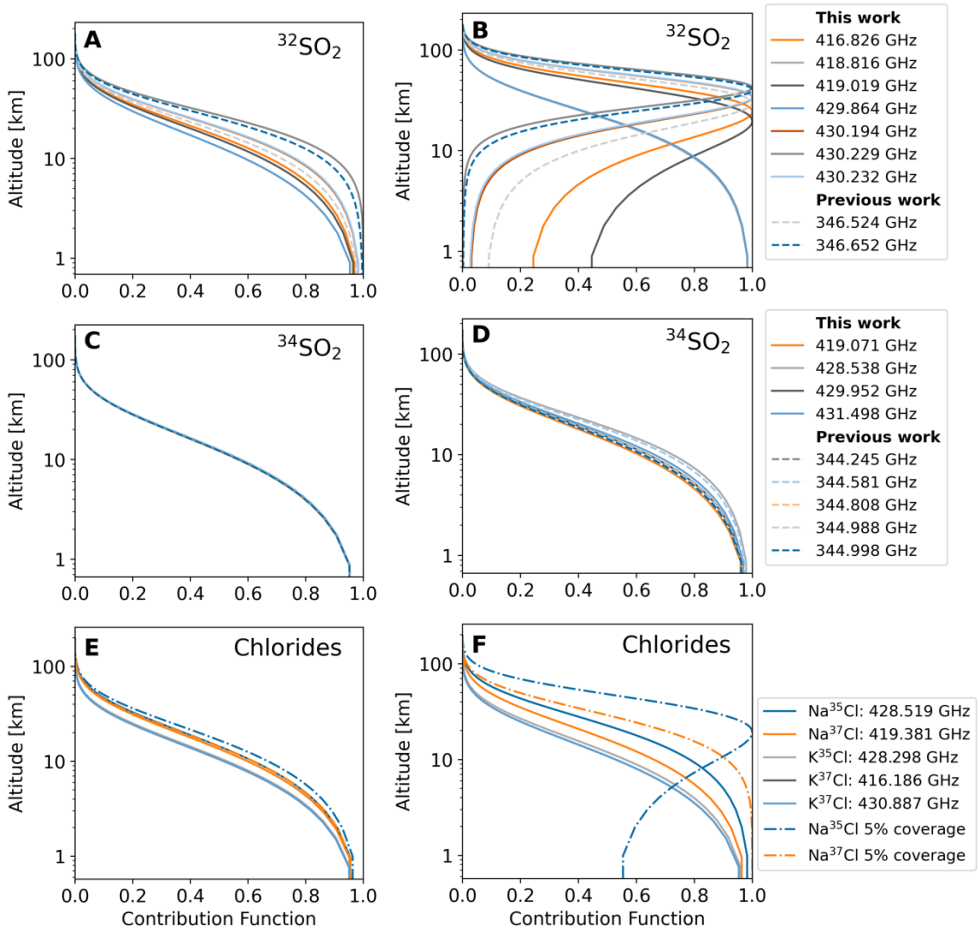

Fig. S3. **Contribution functions for emission lines from this and previous work.** Contribution functions for all observed lines of the species used to derive the sulfur and chlorine isotope ratios. The lines used in previous work (*15*) are shown for comparison. (**A,C,E**) Calculated values for the center of the disk and (**B,D,F**) the limb, for the species indicated on the panels. The SO_2 contribution functions assume an SO_2 column density of $1x10^{16}$ cm^{-2} and gas temperature of 240 K, corresponding to the leading hemisphere best fitting values in Table 1. For $^{32}SO_2$, only the lines at 418.816 and 429.864 GHz are used to derive the isotope ratio because they are sensitive to the same atmospheric altitudes as the $^{34}SO_2$ lines, especially near the limb where much of the emission appears. The NaCl and KCl contribution functions assume a temperature of 800 K and 20% fractional coverage unless otherwise indicated; some contribution functions assume an alternative 5% coverage (for an equivalent disk-integrated column) to show how much the fractional coverage can impact the relative altitudes the isotopologues are sensitive to.

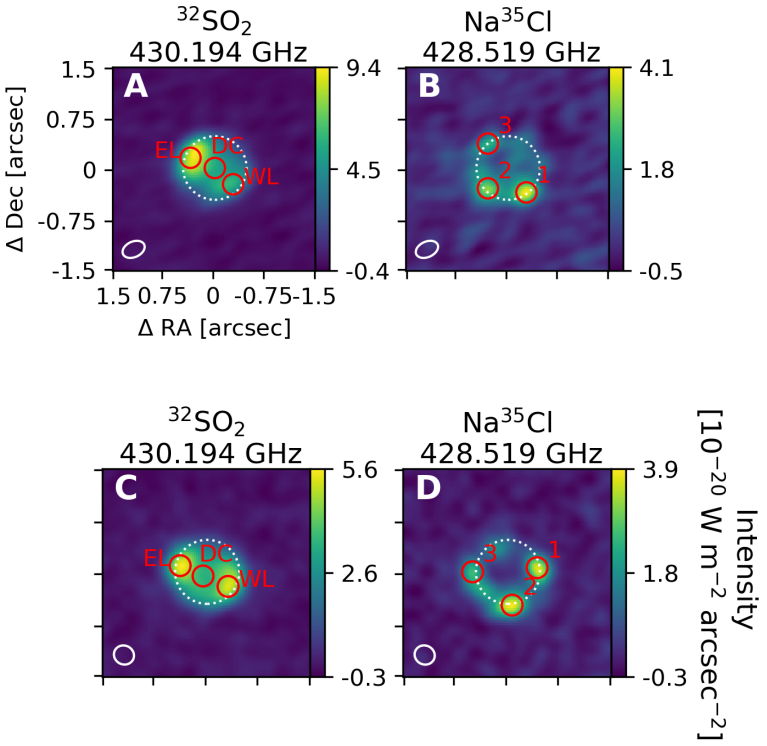

Fig S4. **Locations used for local model fitting.** Images of (**A-B**) the leading and (**C-D**) trailing hemisphere in example emission lines of (**A,C**) $^{32}SO_2$ and (**B,D**) $Na^{35}Cl$ (frequencies labeled above each panel). Red circles indicate the apertures used for our tests (see text). For $^{32}SO_2$, the identified regions are the east limb (EL), west limb (WL), and disk center (DC). For $Na^{35}Cl$, the identified regions are the three brightest emission locations in each observation. Other symbols are the same as in Figure 1.

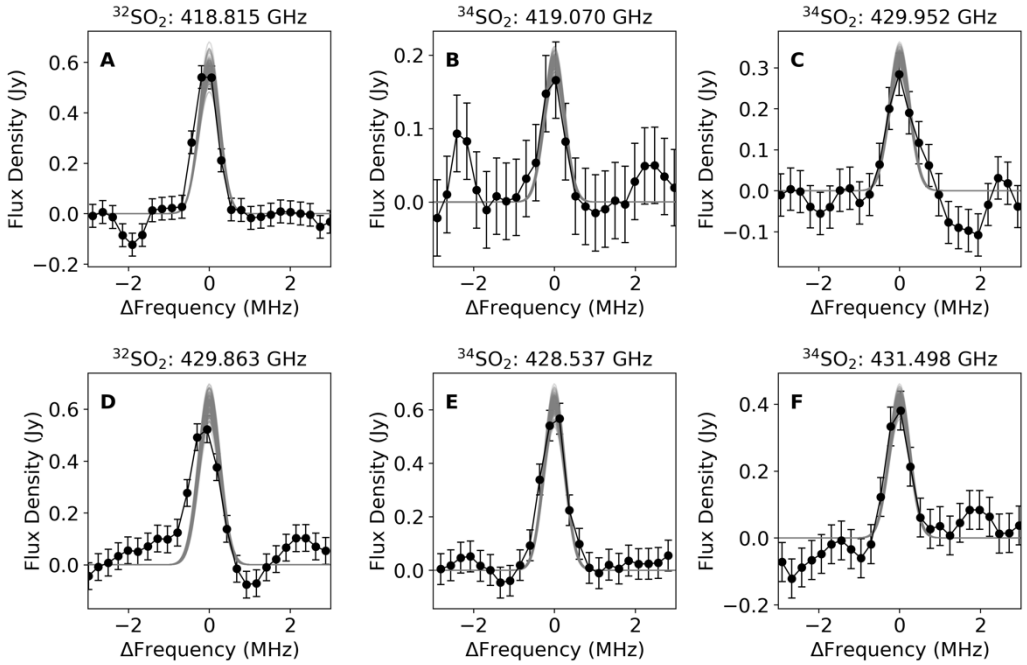

Fig S5. **Visualization of parameter uncertainties.** Same as Fig. 2I-K and M-O but with multiple models (gray curves) corresponding to 150 parameter combinations randomly selected from the joint posterior probability distribution determined by the MCMC simulation.

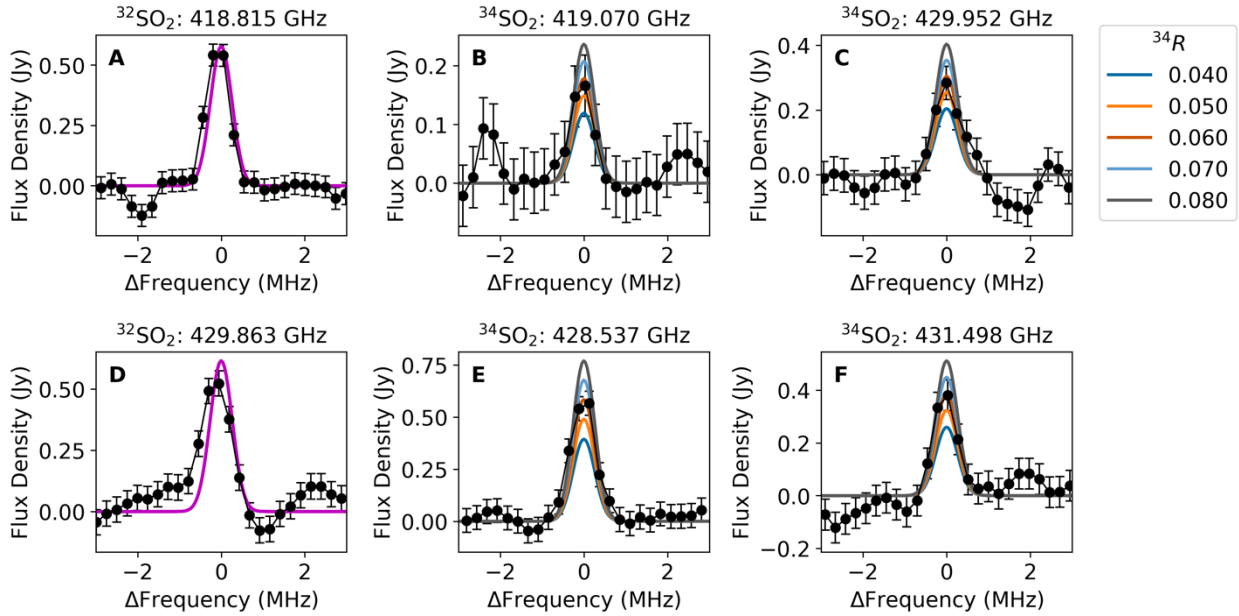

Fig S6. **Visualization of different isotope ratios.** Same as Fig. S5, but with models corresponding to different isotope ratios (see legend). The models shown all adopt the best-fitting $^{32}SO_2$ column density for this observation. The ^{34}R values shown for $^{34}SO_2$ were chosen to be ±5σ from the best fitting value.

Table S1. Observing parameters for the two observations presented in this paper.

Hemisphere	Leading	Trailing
Date/Time [UT]	2022-05-24 12:48 to 16:07	2022-05-18 10:28 to 12:02
Time on Source	1h40m	50m
Precipitable water vapor [mm]	0.7 to 0.8	0.5
Angular resolution	0″.23×0″.35	0″.27×0″.29
Angular Diameter	0″.937	0″.924
Sub-obs longitude [°W]	73 to 101	27 to 287
Sub-obs latitude [°N]	2.1	2.1
North pole angle	335°	335°

Table S2. Molecular data for all emission lines detected in our observations. Quantum numbers (QN) are given for the total rotational quantum number (J), the total rotational angular momentum (N), and the projections of N onto the A and C inertial axes (K_a and K_c respectively), for the upper and lower state. The lower state energy (E_L) is given in cm^{-1}. Data from CDMS (*43, 44*, *53-61*).

Species	Frequency [MHz]	E_L [cm^{-1}]	Line Strength at 300 K [cm^{-1}/(molecule × cm^{-2})]	QN	Detected Leading	Detected Trailing
$^{32}SO_2$	416825.5576±0.0019	289.053	6.87986×10^{-22}	J=28 K_a=4←5 K_c=24←23	Y	Y
$^{32}SO_2$	418815.8002±0.0020	192.736	1.03748×10^{-22}	J=18←17 K_a=7←8 K_c=11←10	Y	Y
$^{32}SO_2$	419019.0378±0.0019	331.436	5.58444×10^{-22}	J=31 K_a=3←4 K_c=29←28	Y	Y
$^{32}SO_2$	429863.8467±0.0019	659.183	1.91637×10^{-22}	J=44 K_a=3←4 K_c=41←40	Y	Y
$^{32}SO_2$	430193.7070±0.0015	180.632	1.05604×10^{-21}	J=23←24 K_a=2←1 K_c=22←23	Y	Y
$^{32}SO_2$	430228.6487±0.0016	168.493	1.66180×10^{-21}	J=23←24 K_a=1←0 K_c=23←24	N/A	Y
$^{32}SO_2$	430232.3126±0.0017	138.228	1.02560×10^{-21}	J=20←21 K_a=1←2 K_c=19←20	N/A	Y
$^{34}SO_2$	419070.9415±0.0056	222.079	5.31348×10^{-22}	J=25←26 K_a=3←2 K_c=23←24	Y	Y
$^{34}SO_2$	428537.9435±0.0065	167.768	1.63448×10^{-21}	J=23←24 K_a=1←0 K_c=23←24	Y	Y
$^{34}SO_2$	429952.4205±0.0075	188.460	8.54829×10^{-22}	J=22 K_a=4←5 K_c=18←17	Y	Y
$^{34}SO_2$	431498.3574±0.0061	179.871	1.07468×10^{-21}	J=23←24 K_a=2←1 K_c=22←23	Y	Y
^{32}SO	431808.196±0.020	67.731	8.78778×10^{-21}	J=9←10 N=10←11	Y	Y
^{34}SO	419640.353±0.014	68.080	6.61728×10^{-21}	J=9←10 N=8←9	Y	N

$Na^{35}Cl$	428518.5512±0.0040	229.071	2.99626×10^{-19}	J=32←33	Y	Y
$Na^{37}Cl$	419381.1264±0.0044	224.178	2.86536×10^{-19}	J=32←33	Y	Y
$K^{35}Cl$	428297.8176±0.0027	393.948	1.58008×10^{-19}	J=55←56	Y	Y
$K^{37}Cl$	416185.8003±0.0027	382.778	1.52012×10^{-19}	J=55←56	Y	N
$K^{37}Cl$	430886.5999±0.0028	410.788	1.47360×10^{-19}	J=57←58	Y	N

Table S3. Best-fitting model parameters for local analysis. Same as Table 1, but for the local regions shown in Fig S4, with 1σ uncertainties from MCMC simulations.

Sulfur-bearing molecules			
Region	SO_2 column density [cm^{-2}]	T_{gas} [K]	$^{34}SO_2/^{32}SO_2$
Leading: EL	$(1.306\pm0.034)\times10^{16}$	238.8±2.9	0.0579±0.0020
Leading: WL	$(7.19\pm0.34)\times10^{15}$	236.8±5.5	0.0574±0.0038
Leading: DC	$(1.971\pm0.090)\times10^{16}$	198.4±4.0	0.0526±0.0028
Trailing: EL	$(3.59\pm0.19)\times10^{15}$	260.5±7.9	0.0659±0.0051
Trailing: WL	$(4.22\pm0.31)\times10^{15}$	240.3±9.4	0.0660±0.0061
Trailing: DC	$(5.61\pm0.55)\times10^{15}$	210.2±9.7	0.0682±0.0081

Chlorine-bearing molecules					
Region	NaCl column density [cm^{-2}]	KCl column density [cm^{-2}]	T_{gas} [K]	$^{37}Cl/^{35}Cl$	Velocity [m s^{-1}]
Leading: 1	$(4.18\pm0.23)\times10^{12}$	$(7.79\pm0.77)\times10^{11}$	934±59	0.405±0.020	19±11
Leading: 2	$(4.99\pm0.23)\times10^{12}$	$(5.3\pm1.4)\times10^{11}$	727±49	0.348±0.021	52±11
Leading: 3	$(2.82\pm0.40)\times10^{11}$	$(4.0\pm1.1)\times10^{10}$	1320±180	0.399±0.044	275±22
Trailing: 1	$(4.38\pm0.13)\times10^{12}$	$(5.4\pm1.1)\times10^{11}$	639±28	0.419±0.018	-90.3±6.4
Trailing: 2	$(7.12\pm0.31)\times10^{11}$	$(7.5\pm1.3)\times10^{10}$	796±42	0.417±0.016	-150±11
Trailing: 3	$(6.21\pm0.62)\times10^{11}$	$(3.7\pm2.1)\times10^{10}$	1290±130	0.350±0.029	-24±15

Table S4. NaCl and KCl source locations and possible identifications with paterae. Location numbers correspond to Figure 1. The most likely patera is identified if there is a clear, isolated patera at the identified latitude and longitude. All other named paterae within the uncertainties on the latitudes and longitudes are also listed. The latitudes and longitudes of leading hemisphere location 1 and trailing hemisphere location 3 are consistent within 1σ of one another so might be the same gas source.

Location	Latitude	Longitude	Most likely patera	Other paterae within uncertainties
Leading hemisphere				
1	27±10ºS	20±14ºW		Kanehekili Fluctus, Cataquil Patera, Uta Patera, Angpetu Patera
2	66±11ºS	136±17ºW		
3	22±10ºN	159±14ºW		Thomagata Patera, Reshef Patera, Surya Patera, Chaac Patera
Trailing hemisphere				
1	58±10ºS	218±17ºW	Kurdalagon Patera	Gabija Patera
2	30±11ºN	211±13ºW	Isum Patera	Susanoo Patera
3	24±10ºS	355±15ºW		many
4	33±12ºN	330±15ºW	Fuchi Patera	Manua Patera
5	59±11ºS	341±15ºW	Creidne Patera	Hiruko Patera, Inti Patera

Table S5. Data sources for previous isotope measurements shown in Fig 4.

	Sample	**Reference**
Sulfur	Solar wind	(*62*)
	Bulk Silicate Earth (BSE)	(*63*)
	Earth sediments	(*64*)
	Earth volcanic gasses	(*65*)
	Lunar melt inclusions (MIs)	(*66*)
	Lunar mare basalts	(*67*)
	Gale crater sediments	(*68*)
	Ordinary chondrites (OC)	(*28*)
	Comet Hale-Bopp H_2S	(*69*)
	Comet Hale-Bopp CS	(*70*)
	Comet 67P/Churyumov-Gerasimenko	(*29*)
	Comet C/2014 Q2 (Lovejoy)	(*71*)
	Comet C/2012 F6 (Lemmon)	(*71*)
	Interstellar medium (ISM)	(*72*)
	Galactic cosmic rays	(*73*)
Chlorine	Venus, HCl gas	(*74*)
	Moon, basalts and soils	(*75, 76*)
	Mars, HCl gas	(*77*)
	Vesta, from apatite in eucrites	(*78*)
	Comet 67P/Churyumov-Gerasimenko, from HCl gas	(*79)*

References and Notes

1. S. J. Peale, M. H. Lee, A primordial origin of the Laplace relation among the Galilean satellites. *Science* **298**, 593–597 (2002). doi:10.1126/science.1076557 Medline

2. K. Batygin, A. Morbidelli, Formation of giant planet satellites. *Astrophys. J.* **894**, 143 (2020). doi:10.3847/1538-4357/ab8937

3. H. Hussmann, T. Spohn, Thermal-orbital evolution of Io and Europa. *Icarus* **171**, 391–410 (2004). doi:10.1016/j.icarus.2004.05.020

4. C. B. Phillips, *Voyager and Galileo SSI Views of Volcanic Resurfacing on Io and the Search for Geologic Activity on Europa,* thesis (The University of Arizona, 2000); https://repository.arizona.edu/handle/10150/289119.

5. T. V. Johnson, A. F. Cook II, I. I. C. Sagan, L. A. Soderblom, Volcanic resurfacing rates and implications for volatiles on Io. *Nature* **280**, 746–750 (1979). doi:10.1038/280746a0

6. V. Dols, P. A. Delamere, F. Bagenal, A multispecies chemistry model of Io's local interaction with the plasma torus. *J. Geophys. Res.* **113**, A09208 (2008). doi:10.1029/2007JA012805

7. Materials and methods are available as supplementary materials.

8. S. Luszcz-Cook, K. de Kleer, kdekleer/Io_mm_RT: Code version for models published in de Kleer et al., *Zenodo* (2024); https://doi.org/10.5281/zenodo.10794511

9. I. de Pater, S. Luszcz-Cook, P. Rojo, E. Redwing, K. Kleer, A. Moullet, ALMA observations of Io going into and coming out of eclipse. *Planet. Sci. J.* **1**, 60–85 (2020). doi:10.3847/PSJ/abb93d

10. E. Lellouch, D. F. Strobel, M. J. S. Belton, M. E. Summers, G. Paubert, R. Moreno, Detection of sulfur monoxide in Io's atmosphere. *Astrophys. J.* **459**, L107–L110 (1996). doi:10.1086/309956

11. M. E. Summers, D. F. Strobel, Photochemistry and vertical transport in Io's atmosphere. *Icarus* **120**, 290–316 (1996). doi:10.1006/icar.1996.0051

12. Y. Endo, Y. Sekine, Y. Ueno, Sulfur mass-independent fractionation during SO_2 photolysis in low-temperature/pressure atmospheres. *Chem. Geol.* **609**, 121064 (2022). doi:10.1016/j.chemgeo.2022.121064

13. A. Moullet, M. A. Gurwell, E. Lellouch, R. Moreno, Simultaneous mapping of SO_2, SO, NaCl in Io's atmosphere with the Submillimeter Array. *Icarus* **208**, 353–365 (2010). doi:10.1016/j.icarus.2010.02.009

14. E. Redwing, I. de Pater, S. Luszcz-Cook, K. de Kleer, A. Moullet, P. M. Rojo, NaCl and KCl in Io's atmosphere. *Planet. Sci. J.* **3**, 238 (2022). doi:10.3847/PSJ/ac9784

15. A. Moullet, E. Lellouch, R. Moreno, M. Gurwell, J. H. Black, B. Butler, Exploring Io's atmospheric composition with APEX: First measurement of $^{34}SO_2$ and tentative detection of KCl. *Astrophys. J.* **776**, 32 (2013). doi:10.1088/0004-637X/776/1/32

16. T. Ding, S. Valkiers, H. Kipphardt, P. De Bièvre, P. D. P. Taylor, R. Gonfiantini, R. Krouse, Calibrated sulfur isotope abundance ratios of three IAEA sulfur isotope reference

materials and V-CDT with a reassessment of the atomic weight of sulfur. *Geochim. Cosmochim. Acta* **65**, 2433–2437 (2001). doi:10.1016/S0016-7037(01)00611-1

17. F. Bagenal, V. Dols, The space environment of Io and Europa. *J. Geophys. Res. Space Phys.* **125**, e27485 (2020). doi:10.1029/2019JA027485

18. E. M. Sieveka, R. E. Johnson, Ejection of atoms and molecules from Io by plasma-ion impact. *Astrophys. J.* **287**, 418–426 (1984). doi:10.1086/162701

19. J. I. Moses, M. Y. Zolotov, B. Fegley, Photochemistry of a volcanically driven atmosphere on Io: Sulfur and oxygen species from a Pele-type eruption. *Icarus* **156**, 76–106 (2002). doi:10.1006/icar.2001.6758

20. E. Hughes, K. de Kleer, J. Eiler, *et al.*, Io's sulfur cycle: Tracking tidal heating by modelling the evolution of sulfur isotopes. *JGR Planets* 10.1029/2023JE008086 (2024).

21. J. Saur, F. M. Neubauer, D. F. Strobel, M. E. Summers, Three dimensional plasma simulation of Io's interaction with the Io plasma torus: Asymmetric plasma flow. *J. Geophys. Res.* **104**, 25105–25126 (1999). doi:10.1029/1999JA900304

22. S. J. Peale, P. Cassen, R. T. Reynolds, Melting of io by tidal dissipation. *Science* **203**, 892–894 (1979). doi:10.1126/science.203.4383.892 Medline

23. T. C. O'Reilly, G. F. Davies, Magma transport on Io: A mechanism allowing a thick lithosphere. *Geophys. Res. Lett.* **8**, 313–316 (1981). doi:10.1029/GL008i004p00313

24. O. L. Kuskov, V. A. Kronrod, Core sizes and internal structure of Earth's and Jupiter's satellites. *Icarus* **151**, 204–227 (2001). doi:10.1006/icar.2001.6611

25. G. Dreibus, H. Palme, B. Spettel, J. Zipfel, H. Wanke, Sulfur and selenium in chondritic meteorites. *Meteoritics* **30**, 439–445 (1995). doi:10.1111/j.1945-5100.1995.tb01150.x

26. W. B. McKinnon, "Formation and early evolution of Io" in *Io After Galileo*, R. M. C. Lopes, J. R. Spencer, Eds. (Springer-Praxis Books, 2007), pp. 61–88. doi:10.1007/978-3-540-48841-5_4

27. C. J. Bierson, F. Nimmo, Explaining the galilean satellites' density gradient by hydrodynamic escape. *Astrophys. J. Lett.* **897**, L43 (2020). doi:10.3847/2041-8213/aba11a Medline

28. X. Gao, M. H. Thiemens, Variations in the isotopic composition of sulfur in enstatite and ordinary chondrites. *Geochim. Cosmochim. Acta* **57**, 3171–3176 (1993). doi:10.1016/0016-7037(93)90301-C

29. U. Calmonte, K. Altwegg, H. Balsiger, J.-J. Berthelier, A. Bieler, J. De Keyser, B. Fiethe, S. A. Fuselier, S. Gasc, T. I. Gombosi, L. Le Roy, M. Rubin, T. Sémon, C.-Y. Tzou, S. F. Wampfler, Sulphur isotope mass-independent fractionation observed in comet 67P/Churyumov-Gerasimenko by Rosetta/ROSINA. *Mon. Not. R. Astron. Soc.* **469** (Suppl_2), S787–S803 (2017). doi:10.1093/mnras/stx2534

30. J. D. Anderson, R. A. Jacobson, E. L. Lau, W. B. Moore, G. Schubert, Io's gravity field and interior structure. *J. Geophys. Res.* **106**, 32963–32969 (2001). doi:10.1029/2000JE001367

31. A. Godon, N. Jendrzejewski, H. G. M. Eggenkamp, D. A. Banks, M. Ader, M. L. Coleman, F. Pineau, A cross-calibration of chlorine isotopic measurements and suitability of seawater as the international reference material. *Chem. Geol.* **207**, 1–12 (2004). doi:10.1016/j.chemgeo.2003.11.019

32. M. Küppers, N. M. Schneider, Discovery of chlorine in the Io torus. *Geophys. Res. Lett.* **27**, 513–516 (2000). doi:10.1029/1999GL010718

33. C. T. Ewing, K. H. Stern, Equilibrium vaporization rates and vapor pressures of solid and liquid sodium chloride, potassium chloride, potassium bromide, cesium iodide, and lithium fluoride. *J. Phys. Chem.* **78**, 1998–2005 (1974). doi:10.1021/j100613a005

34. J. I. Moses, M. Y. Zolotov, B. Fegley, Alkali and chlorine photochemistry in a volcanically driven atmosphere on Io. *Icarus* **156**, 107–135 (2002). doi:10.1006/icar.2001.6759

35. R. S. Park, W. M. Folkner, J. G. Williams, D. H. Boggs, The JPL planetary and lunar ephemerides DE440 and DE441. *Astron. J.* **161**, 105 (2021). doi:10.3847/1538-3881/abd414

36. T. R. Hunter, R. Indebetouw, C. L. Brogan, K. Berry, C.-S. Chang, H. Francke, V. C. Geers, L. Gómez, J. E. Hibbard, E. M. Humphreys, B. R. Kent, A. A. Kepley, D. Kunneriath, A. Lipnicky, R. A. Loomis, B. S. Mason, J. S. Masters, L. T. Maud, D. Muders, J. Sabater, K. Sugimoto, L. Szűcs, E. Vasiliev, L. Videla, E. Villard, S. J. Williams, R. Xue, I. Yoon, The ALMA interferometric pipeline heuristics. *Publ. Astron. Soc. Pac.* **135**, 074501 (2023). doi:10.1088/1538-3873/ace216

37. T. Cornwell, E. B. Fomalont, "Self-calibration" in *Synthesis Imaging in Radio Astronomy II*, G. B. Taylor, C. L. Carilli, R. A. Perley, Eds., Astronomical Society of the Pacific Conference Series, vol. 180 (1999), pp. 187–199.

38. M. P. McMullin, B. Waters, D. Schiebel, W. Young, K. Golap, "CASA architecture and applications" in *Astronomical Data Analysis Software and Systems XVI*, R. A. Shaw, F. Hill, D. J. Bell, Eds., Astronomical Society of the Pacific Conference Series, vol. 376 (2007), pp. 127–130.

39. B. Bean, S. Bhatnagar, S. Castro, J. D. Meyer, B. Emonts, E. Garcia, R. Garwood, K. Golap, J. G. Villalba, P. Harris, Y. Hayashi, J. Hoskins, M. Hsieh, P. Jagannathan, W. Kawasaki, A. Keimpema, M. Kettenis, J. Lopez, J. Marvil, J. Masters, A. McNichols, D. Mehringer, R. Miel, G. Moellenbrock, F. Montesino, T. Nakazato, J. Ott, D. Petry, M. Pokorny, R. Raba, U. Rau, D. Schiebel, N. Schweighart, S. Sekhar, K. Shimada, D. Small, J.-W. Steeb, K. Sugimoto, V. Suoranta, T. Tsutsumi, I. M. van Bemmel, M. Verkouter, A. Wells, W. Xiong, A. Szomoru, M. Griffith, B. Glendenning, J. Kern; The CASA Team, CASA, the Common Astronomy Software Applications for radio astronomy. *Publ. Astron. Soc. Pac.* **134**, 114501 (2022). doi:10.1088/1538-3873/ac9642

40. J. A. Högbom, Aperture synthesis with a non-regular distribution of interferometer baselines. *Astron. Astrophys.* **15** (suppl.), 417–426 (1974).

41. P. Virtanen, R. Gommers, T. E. Oliphant, M. Haberland, T. Reddy, D. Cournapeau, E. Burovski, P. Peterson, W. Weckesser, J. Bright, S. J. van der Walt, M. Brett, J. Wilson, K. J. Millman, N. Mayorov, A. R. J. Nelson, E. Jones, R. Kern, E. Larson, C. J. Carey, İ. Polat, Y. Feng, E. W. Moore, J. VanderPlas, D. Laxalde, J. Perktold, R. Cimrman, I.

Henriksen, E. A. Quintero, C. R. Harris, A. M. Archibald, A. H. Ribeiro, F. Pedregosa, P. van Mulbregt, A. Vijaykumar, A. P. Bardelli, A. Rothberg, A. Hilboll, A. Kloeckner, A. Scopatz, A. Lee, A. Rokem, C. N. Woods, C. Fulton, C. Masson, C. Häggström, C. Fitzgerald, D. A. Nicholson, D. R. Hagen, D. V. Pasechnik, E. Olivetti, E. Martin, E. Wieser, F. Silva, F. Lenders, F. Wilhelm, G. Young, G. A. Price, G.-L. Ingold, G. E. Allen, G. R. Lee, H. Audren, I. Probst, J. P. Dietrich, J. Silterra, J. T. Webber, J. Slavič, J. Nothman, J. Buchner, J. Kulick, J. L. Schönberger, J. V. de Miranda Cardoso, J. Reimer, J. Harrington, J. L. C. Rodríguez, J. Nunez-Iglesias, J. Kuczynski, K. Tritz, M. Thoma, M. Newville, M. Kümmerer, M. Bolingbroke, M. Tartre, M. Pak, N. J. Smith, N. Nowaczyk, N. Shebanov, O. Pavlyk, P. A. Brodtkorb, P. Lee, R. T. McGibbon, R. Feldbauer, S. Lewis, S. Tygier, S. Sievert, S. Vigna, S. Peterson, S. More, T. Pudlik, T. Oshima, T. J. Pingel, T. P. Robitaille, T. Spura, T. R. Jones, T. Cera, T. Leslie, T. Zito, T. Krauss, U. Upadhyay, Y. O. Halchenko, Y. Vázquez-Baeza; SciPy 1.0 Contributors, SciPy 1.0: Fundamental algorithms for scientific computing in Python. *Nat. Methods* **17**, 261–272 (2020). doi:10.1038/s41592-019-0686-2 Medline

42. D. Foreman-Mackey, D. W. Hogg, D. Lang, J. Goodman, emcee: The MCMC hammer. *Publ. Astron. Soc. Pac.* **125**, 306–312 (2013). doi:10.1086/670067

43. H. S. P. Müller, S. Thorwirth, D. A. Roth, G. Winnewisser, The Cologne Database for Molecular Spectroscopy. *Astron. Astrophys.* **370**, L49–L52 (2001). doi:10.1051/0004-6361:20010367

44. C. P. Endres, S. Schlemmer, P. Schilke, J. Stutzki, H. S. P. Müller, The Cologne Database for Molecular Spectroscopy, CDMS, in the Virtual Atomic and Molecular Data Centre, VAMDC, The Cologne Database for Molecular Spectroscopy, CDMS, in the Virtual Atomic and Molecular Data Centre, VAMDC. *J. Mol. Spectrosc.* **327**, 95–104 (2016). doi:10.1016/j.jms.2016.03.005

45. H. M. Pickett, R. L. Poynter, E. A. Cohen, M. L. Delitsky, J. C. Pearson, H. S. P. Müller, Submillimeter, millimeter, and microwave spectral line catalog. *J. Quant. Spectrosc. Radiat. Transf.* **60**, 883–890 (1998). doi:10.1016/S0022-4073(98)00091-0

46. J. Zhang, D. B. Goldstein, P. L. Varghese, N. E. Gimelshein, S. F. Gimelshein, D. A. Levin, Simulation of gas dynamics and radiation in volcanic plumes on Io. *Icarus* **163**, 182–197 (2003). doi:10.1016/S0019-1035(03)00050-2

47. D. A. Williams, L. P. Keszthelyi, D. A. Crown, J. A. Yff, W. L. Jaeger, P. M. Schenk, Geologic map of Io: U.S. Geological Survey Scientific Investigations Map 3168, scale 1:15,000,000 (2011); https://pubs.usgs.gov/sim/3168/.

48. K. de Kleer, I. de Pater, Time variability of Io's volcanic activity from near-IR adaptive optics observations on 100 nights in 2013-2015. *Icarus* **280**, 378–404 (2016). doi:10.1016/j.icarus.2016.06.019

49. The Twilight Zone, W. M. Keck Observatory https://www2.keck.hawaii.edu/inst/tda/TwilightZone.html

50. J. Labidi, A. Shahar, C. Le Losq, V. J. Hillgren, B. O. Mysen, J. Farquhar, Experimentally determined sulfur isotope fractionation between metal and silicate and implications for planetary differentiation. *Geochim. Cosmochim. Acta* **175**, 181–194 (2016). doi:10.1016/j.gca.2015.12.001

51. M. C. Wong, R. E. Johnson, The effect of plasma heating on sublimation-driven flow in Io's atmosphere. *Icarus* **115**, 109–118 (1995). doi:10.1006/icar.1995.1082

52. M. C. Wong, W. H. Smyth, Model calculations for Io's atmosphere at eastern and western elongations. *Icarus* **146**, 60–74 (2000). doi:10.1006/icar.2000.6362

53. P. A. Helminger, F. C. De Lucia, The submillimeter wave spectrum of $^{32}S^{16}O_2$, $^{32}S^{16}O_2(v_2)$, and $^{34}S^{16}O_2$. *J. Mol. Spectrosc.* **111**, 66–72 (1985). doi:10.1016/0022-2852(85)90069-4

54. F. J. Lovas, Microwave spectra of molecules of astrophysical interest. XXII. Sulfur dioxide (SO_2). *J. Phys. Chem. Ref. Data* **14**, 395–488 (1985). doi:10.1063/1.555729

55. E. A. Alekseev, S. F. Dyubko, V. V. Ilyushin, S. V. Podnos, The high-precision millimeter-wave spectrum of $^{32}SO_2$, $^{32}SO_2(v_2)$, and $^{34}SO_2$. *J. Mol. Spectrosc.* **176**, 316–320 (1996). doi:10.1006/jmsp.1996.0092

56. D. Patel, D. Margolese, T. R. Dyke, Electric dipole moment of the SO_2 in ground and excited vibrational states. *J. Chem. Phys.* **70**, 2740–2747 (1979). doi:10.1063/1.437860

57. W. W. Clark, F. C. De Lucia, The microwave spectrum and rotational structure of the $^1\Delta$ and $^3\Sigma$ electronic states of sulfur monoxide. *J. Mol. Spectrosc.* **60**, 332–342 (1976). doi:10.1016/0022-2852(76)90136-3

58. F. X. Powell, D. R. Lide Jr., Microwave spectrum of the SO radical. *J. Chem. Phys.* **41**, 1413–1419 (1964). doi:10.1063/1.1726082

59. E. Tiemann, Microwave spectra of molecules of astrophysical interest. 8. Sulfur monoxide. *J. Phys. Chem. Ref. Data* **3**, 259–268 (1974). doi:10.1063/1.3253141

60. P. L. Clouser, W. Gordy, Millimeter-wave molecular-beam spectroscopy: Alkali chlorides. *Phys. Rev.* **134**, 863–870 (1964). doi:10.1103/PhysRev.134.A863

61. K. H. Hellwege, Ed., Landolt-Börnstein Numerical Data and Functional Relationships in Science and Technology, Group II, Vol. 6, Molecular Constants (Springer-Verlag, 1974).

62. C. Giammanco, P. Wurz, A. Opitz, F. M. Ipavich, J. A. Paquette, Sulfur abundance in the slow solar wind. *Astron. J.* **134**, 2451–2454 (2007). doi:10.1086/523597

63. J. Labidi, J. Farquhar, C. M. O. D. Alexander, D. L. Eldridge, H. Oduro, Mass independent sulfur isotope signatures in CMs: Implications for sulfur chemistry in the early Solar System. *Geochim. Cosmochim. Acta* **196**, 326–350 (2017). doi:10.1016/j.gca.2016.09.036

64. J. Farquhar, B. A. Wing, "The terrestrial record of stable sulphur isotopes: A review of the implications for the evolution of Earth's sulphur cycle" in *Mineral Deposits and Earth Evolution*. *Spec. Publ. Geol. Soc. Lond.* **248**, 167–177 (2005). doi:10.1144/GSL.SP.2005.248.01.09

65. T. Kagoshima, Y. Sano, N. Takahata, T. Maruoka, T. P. Fischer, K. Hattori, Sulphur geodynamic cycle. *Sci. Rep.* **5**, 8330 (2015). doi:10.1038/srep08330 Medline

66. A. E. Saal, E. H. Hauri, Large sulfur isotope fractionation in lunar volcanic glasses reveals the magmatic differentiation and degassing of the Moon. *Sci. Adv.* **7**, eabe4641 (2021). doi:10.1126/sciadv.abe4641 Medline

67. B. A. Wing, J. Farquhar, Sulfur isotope homogeneity of lunar mare basalts. *Geochim. Cosmochim. Acta* **170**, 266–280 (2015). doi:10.1016/j.gca.2015.09.003

68. H. Franz, A. C. McAdam, D. W. Ming, C. Freissinet, P. R. Mahaffy, D. L. Eldridge, W. W. Fischer, J. P. Grotzinger, C. H. House, J. A. Hurowitz, S. M. McLennan, S. P. Schwenzer, D. T. Vaniman, P. D. Archer Jr., S. K. Atreya, P. G. Conrad, J. W. Dottin III, J. L. Eigenbrode, K. A. Farley, D. P. Glavin, S. S. Johnson, C. A. Knudson, R. V. Morris, R. Navarro-González, A. A. Pavlov, R. Plummer, E. B. Rampe, J. C. Stern, A. Steele, R. E. Summons, B. Sutter, Large sulfur isotope fractionations in Martian sediments at Gale crater. *Nat. Geosci.* **10**, 658–662 (2017). doi:10.1038/ngeo3002

69. J. Crovisier, D. Bockelée-Morvan, P. Colom, N. Biver, D. Despois, D. C. Lis, The composition of ices in comet C/1995 OI (Hale-Bopp) from radio spectroscopy: Further results and upper limits on undetected species. *Astron. Astrophys.* **418**, 1141–1157 (2004). doi:10.1051/0004-6361:20035688

70. D. Jewitt, H. E. Matthews, T. Owen, R. Meier, The 12C/13C, 14N/15N and 32S/34S isotope ratios in comet Hale-Bopp (C/1995 OI). *Science* **278**, 90–93 (1997). doi:10.1126/science.278.5335.90 Medline

71. N. Biver, R. Moreno, D. Bockelée-Morvan, A. Sandqvist, P. Colom, J. Crovisier, D. C. Lis, J. Boissier, V. Debout, G. Paubert, S. Milam, A. Hjalmarson, S. Lundin, T. Karlsson, M. Battelino, U. Frisk, D. Murtagh, Isotopic ratios of H, C, N, O, and S in comets C/2012 F6 (Lemmon) and C/2014 Q2 (Lovejoy). *Astron. Astrophys.* **589**, A78 (2016). doi:10.1051/0004-6361/201528041

72. Y.-N. Chin, C. Henkel, J. B. Whiteoak, N. Langer, E. B. Churchwell, Interstellar sulfur isotopes and stellar oxygen burning. *Astron. Astrophys.* **305**, 960–969 (1996). doi:10.48550/arXiv.astro-ph/9505067

73. M. R. Thayer, An investigation into sulfur isotopes in the galactic cosmic rays. *Astrophys. J.* **482**, 792–795 (1997). doi:10.1086/304173

74. N. Iwagami, S. Ohtsuki, K. Tokuda, N. Ohira, Y. Kasaba, T. Imamura, H. Sagawa, G. L. Hashimoto, S. Takeuchi, M. Ueno, S. Okumura, Hemispheric distributions of HCl above and below the Venus' clouds by ground-based 1.7 μm spectroscopy. *Planet. Space Sci.* **56**, 1424–1434 (2008). doi:10.1016/j.pss.2008.05.009

75. J. J. Barnes, I. A. Franchi, F. M. McCubbin, M. Anand, Multiple reservoirs of volatiles in the Moon revealed by the isotopic composition of chlorine in lunar basalts. *Geochim. Cosmochim. Acta* **266**, 144–162 (2019). doi:10.1016/j.gca.2018.12.032

76. C. K. Shearer, Z. D. Sharp, P. V. Burger, F. M. McCubbin, P. P. Provencio, A. J. Brearley, A. Steele, Chlorine distribution and its isotopic composition in "rusty rock" 66095. Implications for volatile element enrichments in "rusty rock" and lunar soils, origin of "rust" alteration, and volatile element behavior on the Moon. *Geochim. Cosmochim. Acta* **139**, 411–433 (2014). doi:10.1016/j.gca.2014.04.029

77. G. Liuzzi, G. L. Villanueva, S. Viscardy, D. Mège, M. M. J. Crismani, S. Aoki, J. Gurgurewicz, P.-A. Tesson, M. J. Mumma, M. D. Smith, S. Faggi, V. Kofman, E. W. Knutsen, F. Daerden, L. Neary, F. Schmidt, L. Trompet, J. T. Erwin, S. Robert, I. R. Thomas, B. Ristic, G. Bellucci, J. J. Lopez-Moreno, M. R. Patel, A. C. Vandaele, Probing

the atmospheric Cl isotopic ratio on Mars: Implications for planetary evolution and atmospheric chemistry. *Geophys. Res. Lett.* **48**, e2021GL092650 (2021). doi:10.1029/2021GL092650

78. T. J. Barrett, J. J. Barnes, M. Anand, I. A. Franchi, R. C. Greenwood, B. L. A. Charlier, X. Zhao, F. Moynier, M. M. Grady, Investigating magmatic processes in the early Solar System using the Cl isotopic systematics in eucrites. *Geochim. Cosmochim. Acta* **266**, 582–597 (2019). doi:10.1016/j.gca.2019.06.024

79. F. Dhooghe, J. De Keyser, K. Altwegg, C. Briois, H. Balsiger, J.-J. Berthelier, U. Calmonte, G. Cessateur, M. R. Combi, E. Equeter, B. Fiethe, N. Fray, S. Fuselier, S. Gasc, A. Gibbons, T. Gombosi, H. Gunell, M. Hässig, M. Hilchenbach, L. Le Roy, R. Maggiolo, U. Mall, B. Marty, E. Neefs, H. Rème, M. Rubin, T. Sémon, C.-Y. Tzou, P. Wurz, Halogens as tracers of protosolar nebula material in comet 67P/Churyumov-Gerasimenko. *Mon. Not. R. Astron. Soc.* **472**, 1336–1345 (2017). doi:10.1093/mnras/stx1911